HHS Public Access

Author manuscript

Magn Reson Med. Author manuscript; available in PMC 2017 December 01.

Published in final edited form as:

Magn Reson Med. 2016 December ; 76(6): 1750–1763. doi:10.1002/mrm.26071.

Q-Space Truncation and Sampling in Diffusion Spectrum Imaging

Qiyuan Tian[1,2,*], **Ariel Rokem**[3], **Rebecca D. Folkerth**[4], **Aapo Nummenmaa**[5], **Qiuyun Fan**[5], **Brian L. Edlow**[5,6], and **Jennifer A. McNab**[2]

[1]Department of Electrical Engineering, Stanford University, Stanford, California, USA.

[2]Department of Radiology, Stanford University, Stanford, California, USA.

[3]Department of Psychology, Stanford University, Stanford, California, USA.

[4]Department of Pathology, Brigham and Women's Hospital, Boston, Massachusetts, USA.

[5]Athinoula A. Martinos Center for Biomedical Imaging, Massachusetts General Hospital, Charlestown, Massachusetts, USA.

[6]Department of Neurology, Massachusetts General Hospital, Boston, Massachusetts, USA.

Abstract

Purpose—To characterize the q-space truncation and sampling on the spin-displacement probability density function (PDF) in diffusion spectrum imaging (DSI).

Methods—DSI data were acquired using the MGH-USC connectome scanner (G_{max}=300mT/m) with b_{max}=30,000s/mm^2, 17×17×17, 15×15×15 and 11×11×11 grids in *ex vivo* human brains and b_{max}=10,000s/mm^2, 11×11×11 grid *in vivo*. An additional *in vivo* scan using b_{max}=7,000s/mm^2, 11×11×11 grid was performed with a derated gradient strength of 40mT/m. PDFs and orientation distribution functions (ODFs) were reconstructed with different q-space filtering and PDF integration lengths, and from down-sampled data by factors of two and three.

Results—Both *ex vivo* and *in vivo* data showed Gibbs ringing in PDFs, which becomes the main source of artifact in the subsequently reconstructed ODFs. For down-sampled data, PDFs interfere with the first replicas or their ringing, leading to obscured orientations in ODFs.

Conclusion—The minimum required q-space sampling density corresponds to a field-of-view approximately equal to twice the mean displacement distance (MDD) of the tissue. The 11×11×11 grid is suitable for both *ex vivo* and *in vivo* DSI experiments. To minimize the effects of Gibbs ringing, ODFs should be reconstructed from unfiltered q-space data with the integration length over the PDF constrained to around the MDD.

Keywords

Diffusion spectrum imaging; q-space truncation and sampling; Gibbs ringing artifacts; aliasing artifacts; *ex vivo* imaging; high b-value

[*]Correspondence to: Qiyuan Tian, Ph. D. Candidate, Department of Electrical Engineering, Stanford University, Richard M. Lucas Center for Imaging, 1201 Welch Road, Stanford, California, USA, 94305. qytian@stanford.edu.

INTRODUCTION

The advent and widespread adoption of diffusion tensor imaging (DTI) (1, 2) in the 1990's was concurrent with improvements in magnetic resonance imaging (MRI) gradient specifications that enabled single-shot read-outs that allow whole-brain measurements in reasonable scan-times, and confer robustness against motion artifacts. Recently, dramatic improvements in gradient technology for human scanners (3-8) have enabled further increases in gradient amplitudes that once again provide new opportunities to exploit the diffusion MRI signal. Namely, the increased maximum gradient amplitudes are making high b-value methods such as diffusion spectrum imaging (DSI) (9) more feasible in the *in vivo* human brain. Here, we aim to characterize the q-space truncation and sampling in DSI using unique *in vivo* and *ex vivo* human brain DSI data acquired on the 3T MGH-USC connectome scanner.

DSI is one approach proposed to resolve intra-voxel crossing fibers, which have been observed throughout the human brainstem (10) and cerebral hemispheres (11, 12). Although DTI can accurately estimate a single fiber orientation, it fails to delineate multiple intra-voxel orientations, thus limiting its utility in studying complex fiber configurations and accurately tracing fiber pathways. DSI is based on the Fourier relationship between the attenuated echo signal in q-space and the spin-displacement probability density function (PDF) (13, 14). In DSI, q-space is most commonly sampled on a Cartesian grid extending to a sphere with a radius equal to the maximum q-value ($q_{\max}$). By analogy to normal k-space imaging (15), q-space coverage determines the PDF resolution ($1/2q_{\max}$), i.e. the ability to differentiate between different spin-displacement lengths, while q-space sampling density determines the field-of-view (FOV) in the PDF domain ($1/\Delta q$). An insufficient q-space coverage and sampling density can create Gibbs ringing artifacts and aliasing artifacts respectively in the reconstructed PDF (16).

The PDF represents the density of the average spin displacement in a voxel, is therefore also called ensemble average propagator or diffusion propagator (17). In order to simplify its angular structure, a radial projection of the PDF is taken to generate the orientation distribution function (ODF). ODFs are then used to reconstruct white matter pathways in the brain (i.e. fiber tractography) (18-20). DSI in conjunction with tractography has been used extensively and was recently used to propose a new theory regarding the fundamental geometric structure of hemispheric fiber pathways (21).

DSI has been studied previously in terms of the optimal maximum b-value (22), q-space sampling density (23, 24) and pattern (25-28), q-space truncation (29-32) and reconstruction methods (33-36). These prior studies have focused predominantly on the ODF and tractography results when developing and evaluating methods. In contrast, our study characterizes the q-space sampling density and ODF reconstruction by analyzing the spin-displacement PDF.

The PDF is the direct result of the Fourier transform of the acquired q-space data. Therefore, the PDF displays the immediate effects of different q-space signal acquisition schemes. ODF and tractography results are computed using various algorithms and therefore are one step

removed from the q-space acquisition. Namely, the ODF is reconstructed via a radial projection of the PDF. Studying the PDF provides more direct assessment of the source of artifacts and informs ODF reconstruction methods. Further, the PDF itself provides rich information about the microstructural properties of the tissue and many NMR and MRI works have studied the optimal methods to obtain accurate PDF and related measures (30, 32, 37-41).

Using the MGH-USC connectome scanner for data acquisition provides several advantages. The high gradient strength (up to 300 mT/m) achieves a higher maximum b-value in shorter gradient durations, which brings our experiments closer to the narrow pulse approximation and improves signal-to-noise ratio (SNR). The MGH-USC connectome scanner also enables acquisition of *ex vivo* DSI data on a whole, fixed human brain. Previously, *ex vivo* DSI experiments have been performed predominantly in animal brains (21, 42, 43) since a whole, fixed human brain does not fit in a small-bore animal MRI unit that has conventionally been the only system with sufficiently strong gradients. *Ex vivo* imaging in itself is of great interest to many research groups because it provides gold-standard data at ultra-high resolution and enables comparison with histology in the same specimen (44-48). *Ex vivo* DSI can provide very high quality data because it is devoid of motion and enables long scan time such that many samples may be acquired to increase SNR and q-space sampling density.

In this study, we focus on characterizing the effects of q-space truncation and sampling on the PDF for a DSI acquisition. For q-space truncation, we demonstrate the presence of Gibbs ringing in the PDF and investigate different methods to mitigate the ringing. We approximate the PDF extent using the mean displacement distance (MDD) of the tissue and constrain the integration length over the PDF to the MDD to avoid ringing in the PDF from translating into the ODF. For q-space sampling density, we explore how the determined FOV compares to the PDF extent. Using down-sampled data, we demonstrate how the PDF is affected by aliasing and when the aliasing artifacts obscure information in the ODF.

METHODS

Data Acquisition

Ex vivo and *in vivo* data were acquired with Institutional Review Board (IRB) approval. Written informed consent was provided by healthy control subjects for *in vivo* imaging and by next-of-kin for *ex vivo* imaging. All data were acquired using the MGH-USC connectome scanner (3T MAGNETOM CONNECTOM, Siemens Healthcare). The scanner consists of a novel AS302 gradient system capable of producing gradients of up to 300 mT/m at a slew rate of up to 200 T/m/s. A custom-built 64-channel RF receive coil was used for signal acquisition (49). A 2D single-refocused diffusion-weighted SE-EPI sequence was used to acquire three *ex vivo* datasets in a single whole, human brain specimen and two *in vivo* datasets from healthy human subjects. The data acquisition parameters are shown in Table 1 and example diffusion-weighted images (DWIs) are shown in Fig. 1.

Ex vivo data was required on one whole, fixed human brain (14-hour post-mortem interval, 7 months fixation) from a 58-year-old woman who died of non-neurological causes. For

imaging, the brain specimen was immersed in a non-protonated solution called fomblin (perfluoropolyether, Ausiomont USA Inc., Thorofare, NJ). Three *ex vivo* datasets were acquired with the same q_{max} =178.6 mm^{-1} (equivalent to b_{max}=30,000 s/mm^2 given the diffusion time (Δ) and gradient pulse duration (δ) used in the experiments) but different q-space grid sizes (17×17×17, 15×15×15 and 11×11×11). These Cartesian grids in q-space will be referred to herein as DSI-17, DSI-15 and DSI-11. A larger b_{max} was used for the *ex vivo* acquisitions to compensate for the slower diffusion rates in *ex vivo* tissue. The larger *ex vivo* b_{max} results in longer TE, TR and Δ values because the diffusion encoding gradients must be longer in duration to achieve the higher b_{max}. Non-diffusion-weighted (b=0 s/mm^2) images were interleaved between every 17 DWIs for the DSI-17 dataset and between every 16 DWIs for DSI-15 and DSI-11 datasets. There were 124, 102, 37 non-diffusion-weighted images in total for DSI-17, DSI-15 and DSI-11, respectively. Positive and negative gradient pairs from the q-space lattice were acquired sequentially.

Two *in vivo* datasets were acquired in a healthy 23-year-old male volunteer and a 24-year-old female volunteer using the DSI-11 sampling protocol. A high gradient strength of 225 mT/m was used to acquire the dataset DSI-11-Gmax225 with q_{max}=123.5 mm^{-1} (equivalent to b_{max}=10,000 s/mm^2). A commonly used gradient strength of 40 mT/m was used to acquire the dataset DSI-11-Gmax40 with q_{max}=71.1 mm^{-1} (equivalent to b_{max}=7,000 s/mm^2). Non-diffusion-weighted images were interspersed every 16 DWIs. There were 33 non-diffusion-weighted images in total. For DSI-11-Gmax225, positive and negative gradient pairs from the q-space lattice were acquired sequentially.

Data Processing

For the three *ex vivo* datasets and DSI-11-Gmax225 *in vivo* data, DWI opposite polarity pairs were registered one to the other, constraining for the expected translations, dilations and shears and then the “half-way” transform was calculated to correct eddy current distortions (50). Linear transformations calculated from the interspersed non-diffusion-weighted images were used to correct for effects of magnetic field drift and (for the *in vivo* data) bulk motion between image volumes that was not as easily detected in the DWIs with lower signal-to-noise ratio (SNR). The three *ex vivo* datasets were co-registered. All transformations were applied in a single step to prevent unnecessary blurring using the linear registration tool provided by the FMRIB Software Library (FSL, www.fmrib.ox.ac.uk/fsl) called “FLIRT” (51). For the DSI-11-Gmax40 *in vivo* data, an FSL function called “EDDY_CORRECT” was used to correct eddy current distortions, field drift and bulk motion.

Two ROIs in the *ex vivo* and *in vivo* datasets were selected. One is a 2×4 voxel region located in the center of the corpus callosum (CC) with known left-right principal diffusion orientation. The other is a 5×9 voxel region located in the centrum semiovale that contains the intersection of three white matter bundles: the CC, the corona radiata (CR) and the superior longitudinal fasciculus (SLF).

DSI reconstruction followed the procedures described in (9) and was modified based on the object “DiffusionSpectrumModel” of the Diffusion Imaging in Python (DIPY, http://nipy.org/dipy/) software (52). Specifically, the q-space data were first placed in a cubic grid.

A window function was applied to the q-space data to ensure a smooth attenuation of the signal at the edge of q-space to mitigate Gibbs ringing artifacts. The q-space grid was zero-padded such that the calculated PDF is represented by a sufficiently dense grid. The PDF is computed by performing a 3D Fast Fourier Transform of the zero-padded q-space data and taking the real and non-negative parts of the resulting transform, as the diffusion signal is real, non-negative and symmetric (9, 39, 53). Finally, the ODF is computed as the radial summation of the weighted PDF by the square or higher powers of the displacement distance (9, 54).

The analysis in the following sections was conducted using Python in the IPython interactive computing environment (55) and DIPY software. The raw data for the selected ROIs and the implementation of the analysis that led to each of the figures are available on Github (see https://github.com/mcnablab/DSIQspace).

Extent of the Probability Density Function

To investigate whether the FOV, determined by the q-space sampling density, is sufficiently large, we studied the extent of the PDF. Unlike a physical object with bounded size, a spin-displacement PDF measures the probability of a spin being displaced a specific distance along a specific orientation. Thus, its "extent" is not well defined. We used the mean displacement distance (MDD) given the apparent diffusion coefficient (ADC) measured parallel to the CC as an upper bound of the PDF extent. Assuming Gaussian diffusion, the MDD is equal to the standard deviation of the Gaussian distribution and can be calculated following Einstein's equation (56, 57) as:

$$MDD = \sqrt{6D\left(\Delta - \frac{\delta}{3}\right)} \quad (1)$$

where D is the ADC parallel to the CC, Δ is the experimental diffusion time and δ is the duration of one of the diffusion gradient pulses. D was estimated by fitting data from the CC to the diffusion tensor model using the "DTIFIT" function in FSL (51) and taking the mean of the principal eigenvalues (i.e. the ADC along the principal orientation). In order to have a sufficient number of diffusion weighting directions for tensor model fitting, DWIs with b-values up to 3,000 s/mm^2, 2,000 s/mm^2 and 1,680 s/mm^2 were used for this estimation for the *ex vivo* DSI-17, *in vivo* DSI-11-Gmax225 and DSI-11-Gmax40 data respectively. For the *ex vivo* data, *ex vivo* DSI-17 was used for the estimation of the ADC parallel to the CC since it has more DWIs with b-values under 3,000 s/mm^2 compared to the other two.

Improving ODF Reconstruction

To investigate how Gibbs ringing in a PDF translates to the subsequently reconstructed ODF and to determine how to mitigate these effects, ODFs were calculated on example voxels from the CC ROI and crossing-fiber ROI of the *ex vivo* and *in vivo* DSI-11 data using three different reconstruction pipelines. The pipelines were:

(1) Unfiltered q-space and integration of the PDF to the full FOV;

(2) Filtered q-space and integration of the PDF to the full FOV;

(3) Unfiltered q-space and integration of the PDF to the estimated MDD.

For pipeline (2), three different filters were tested:

$$\text{Hanning window: } h(n) = 0.5 + 0.5 \cdot \cos(2\pi n / W)$$

$$\text{Hamming window: } h(n) = 0.54 + 0.46 \cdot \cos(2\pi n / W)$$

$$\text{Blackman window: } h(n) = 0.42 + 0.5 \cdot \cos(2\pi n / W) + 0.08 \cdot \cos(4\pi n / W)$$

where n is the discrete distance of a q-space point to the origin in the q-space grid and W is the window width. For DSI-11 data, n equals to 0, 1, 2, 3, 4, 5 and W is selected as 10. The roll-off weights equal to 0, 0.08 and 0 at q_{max} for the Hanning, Hamming and Blackman windows respectively.

We also displayed the weighted PDF by the square of displacement distance, and further examined the effect of weighting the PDF using even higher powers of displacement distance to enhance the contributions of faster diffusing components on the reconstructed ODFs. The orientations determined by the local maximas (peaks) of ODFs were visualized to demonstrate the how the ODF influences tractography. The ODF peaks were detected using the DIPY object “peaks_from_model”. The deterministic tractography was performed using the DIPY object “LocalTracking” with default parameters and the centrum semiovale ROI as a seed mask. The generated streamlines were visualized in TrackVis software (http://trackvis.org). Exclusion masks were drawn to exclude the cingulum and contralateral tracts for ease of interpretation.

Q-space Sampling Density Requirement

To explore the q-space sampling density requirement, we down-sampled the data to simulate various sampling densities and examined the potential aliasing artifacts in the PDF and their effects on the subsequently reconstructed ODF. Specifically, we down-sampled all three *ex vivo* data and DSI-11-Gmax225 *in vivo* data by a factor of 2 and 3 in the CC ROI. Down-sampling was performed by preserving every other 2 or 3 q-space points from the center of q-space while replacing the signal in other positions with zeros. Using this down-sampling scheme, the spatial extent over which the PDF is plotted is kept constant and PDF replicas can be therefore visualized. The data at the maximum b-value were preserved in all cases to maintain a constant q_{max}. The ODF reconstruction was performed on the unfiltered q-space with integration of the weighted PDF by the square of displacement distance to the estimated MDD. When the FOV of the down-sampled data is smaller than the MDD, the integration over the PDF only extends to the FOV.

RESULTS

Extent of the Probability Density Function

Fig. 2 depicts coronal cross-sections through the center of the 3D spin-displacement PDF of voxels from the CC ROI (left) and the superior-inferior (S-I) and left-right (L-R) profiles through the center of the cross-sections (right). The PDF was computed from raw q-space data without windowing. One typical voxel from DSI-11 *ex vivo* and *in vivo* data are depicted. The red dashed circles over the PDF cross-sections (left) and the red dashed

rectangles over the PDF profiles (right) represent the approximated extent of PDFs, with their radii being the estimated MDDs. The MDDs are 5.1 μm, 11.9 μm and 18.6 μm for the DSI-11 *ex vivo*, DSI-11-Gmax225 and DSI-11-Gmax40 *in vivo* data, respectively, calculated using the estimated ADCs parallel to the CC of 1.8×10^{-4} mm^2/s, 1.4×10^{-3} mm^2/s and 1.6×10^{-3} mm^2/s. As a reference, assuming a free water diffusion rate of 2.51×10^{-3} mm^2/s (58), the MDDs are 18.9 μm, 15.8 μm and 23.0 μm with the diffusion times and gradient durations employed in the *ex vivo* and *in vivo* experiments. These approximated extents of the PDF are visually consistent with the spin displacements observed in the depicted PDF computed by Fourier transform. For the *ex vivo* data (Fig. 2a), the MDD includes all of the spin displacements along both the principal orientation (L-R) and its perpendicular orientation (S-I). For the *in vivo* data (Fig. 2b and c), the estimated MDD includes most of the spin displacements along the principal orientation (L-R). Since the diffusion rates and the displacement distances are much smaller in the orientation perpendicular to the principal orientation (S-I), the estimated MDD is larger than the PDF extents and even includes the ringing.

Fig. 2 depicts that the FOVs are all sufficiently large to hold the entire PDFs. For DSI-11 *ex vivo*, DSI-11-Gmax225 and DSI-11-Gmax40 *in vivo* data, the q-space sampling densities correspond to FOVs ($=1/\Delta q$) of 28.0 μm, 40.5 μm and 70.3μm respectively, which are 2.7, 1.7 and 1.9 times of the approximated PDF extent (2×MDD). The FOVs for the *ex vivo* data are relatively large compared to the short displacement distances in *ex vivo* tissue. Therefore, the majority of the area within the FOV contains Gibbs ringing with only a small fraction of the FOV containing PDF signals.

Improving ODF Reconstruction

In Fig. 2, although negative values in the PDFs were clipped to 0 in an attempt to remove Gibbs ringing, the positive values of the ringing still remain for both *ex vivo* and *in vivo* data (Fig. 2 white arrows). The S-I profiles (blue curves) and L-R profiles (green curves) through the center of the cross-sections demonstrate the ringing more clearly (Fig. 2 right column). The ringing extends throughout the entire FOV. The magnitude of the ringing is relatively small compared to the PDF peak. The amplitude of the first and second side lobe of S-I profiles is about 5% of the peak.

Fig. 3 demonstrates the effects of applying a filter to q-space data and modifying the distance over which the PDF is integrated (white circles in Fig. 3) on the ODF.

(1) Unfiltered q-space and integration of the PDF to the full FOV—In Fig. 3 rows i, vi and xi, PDFs that were computed from the raw (unfiltered) q-space signal suffer from Gibbs ringing for all *ex vivo* and *in vivo* data. The common practice of weighting the PDF by the square of diffusion distance (9) further enhances ringing and noise at the edges of the PDF (Fig. 3, rows i, vi and xi, columns b and f). The enhanced ringing and noise in the PDFs translates into artifacts in the reconstructed ODF, if these parts of the PDF are included in the PDF integration (i.e. if the integration is performed across the full FOV). The resultant ODFs are noisy (Fig. 3, rows i, vi and xi, columns c and g) and could erroneously indicate

crossing fibers for the single fiber (Fig. 3, rows i, vi and xi, column d) and orientation information is lost for the crossing fiber (Fig. 3, rows i, vi and xi, column h).

(2) Filtered q-space and integration of the PDF to the full FOV—In Fig. 3, rows ii to iv, vii to ix and xii to xiv, the common practice of applying a window to the q-space signal substantially suppresses the ringing and the resultant PDFs are smoother for all the *ex vivo* and *in vivo* data. However, if the PDFs are weighted by the displacement distance, the remaining Gibbs ringing that has not been completely suppressed by the window are again enhanced (Fig. 3, rows ii to iv, vii to ix and xii to xiv, columns b and f). Integrating the PDF from filtered q-space to the full FOV still includes these enhanced ringing artifacts and therefore the resultant ODFs become slightly smoother but still obscure the orientation information, with the exception for the single fiber in the two *in vivo* data (Fig. 3, rows vii to ix and xii to xiv, column d).

(3) Unfiltered q-space and integration of the PDF to the estimated MDD—In Fig. 3, rows v, x and xv, constraining the integration length over the PDF to the estimated MDD avoids most of the ringing and noise at the edge of the PDF while covering the majority of the spin displacements. Therefore, the resultant ODFs clearly indicate the left-right principal diffusion orientation for the single fiber (Fig. 3, rows v, x and xv, column d) and the expected orientations for the intra-voxel crossing fibers (Fig. 3, rows v, x, and xv, column h). For the *in vivo* data, the ODF anisotropy is the highest since the q-space signal is not low-pass filtered using a window function (Fig. 3, rows x and xv, columns g and d). For the *ex vivo* data, the ODF is much cleaner without erroneous peaks (Fig. 3, row v, columns g and h).

Fig. 4 demonstrates the effects of weighting the PDF by different powers, i.e. 0, 1, 2, 4 and 8, of the displacement distance. Using higher powers of the displacement distance enhances the contributions of faster diffusing components and thereby sharpens the ODFs. This sharpening is only possible after limiting the integration length to the estimated MDD, which excludes the ringing artifacts and noise at the edges of the PDF. Otherwise, the ringing artifacts and noise would be significantly enhanced. Since the *in vivo* data has higher anisotropy, the commonly used power of 2 of displacement distance is sufficient for the ODF reconstruction. For the *ex vivo* data, a higher power than 2 is preferred.

ODF results from the centrum semiovale using unfiltered q-space signal and a weighted PDF integration to the MDD are shown in Fig. 5e, f and g. The PDF is weighted by the displacement distance to the power of 8 for the *ex vivo* data and to the power of 2 for the two *in vivo* data. The reconstructed ODFs depict sufficient anisotropy to resolve the expected intra-voxel crossing fibers in the centrum semiovale, i.e. the CC, CR and SLF.

Fig. 6. compares tractography results from ODFs created using the three reconstruction pipelines. Visual analysis of the tractography results demonstrates that the filters greatly decrease the number of false positive tracts. The method of constraining the PDF integration to the MDD produces streamlines that appear to have fewer false positive streamline trajectories than the alternative methods. Additionally, multiple “dead-end” truncated fiber tracts are observed at the site where the CC, SLF and corticospinal tract (CST) cross (white

arrows) in all of the techniques except the technique of constraining the PDF integration distance to the MDD.

Q-Space Sampling Density Requirement

Fig. 7 demonstrates the effects of different q-space sampling densities on the PDF, ODF and ODF peaks. The down-sampling operation decreases the FOV in the PDF domain (Fig. 7, columns a and e, white boxes). For DSI-17 and DSI-15 *ex vivo* data, even with the highest down-sampling rate of 3, the reduced FOVs of size 14.9 μm and 13.1 μm respectively, are still larger than twice the MDD 10.2 μm (comparing white boxes and red dashed circles in Fig. 7, row iii, columns a and e). For DSI-11 *ex vivo* data, the FOV for 2× down-sampling is also larger than twice the MDD (14.0 μm versus 10.4 μm). In these cases, the PDF (set by the approximated extent of MDD) and its replicas do not overlap. Unfortunately, the orientation information in the ODF is still obscured because the ringing from the first PDF replicas overlaps with the desired PDF. When the FOV is larger, the artifacts are less severe since the portion of ringing that enters the desired PDF has lower magnitude (comparing DSI-17 to DSI-15 and DSI-11 *ex vivo*). In the most severe cases, the artifacts create a false representation of fibers along the three orthogonal q-space axes in the resulting ODF (Fig. 7, row iii, columns g and h).

DSI-11-Gmax225 *in vivo* data has a higher diffusion rate and larger displacement, therefore even for the lowest down-sampling rate of 2, the FOV becomes smaller than the PDF extent (20.3 μm versus 23.8μm). The 3× down-sampled DSI-11 *ex vivo* data also has a smaller FOV than the PDF extent (9.3 μm versus 10.2 μm). In these cases, aliasing artifacts can be observed in the PDF (highlighted by the white arrows in Fig. 7). The aliasing artifacts in the PDF obscure the orientation in the ODFs (Fig. 7, rows v and vi, columns g and h) and create three artifactual orthogonal orientations in the worst case (Fig. 7, row vi, columns c and d).

DISCUSSION

Extent of the Probability Density Function

A good approximation of the PDF extent is critical for determining the q-space sampling rate and guiding the ODF reconstruction. The Fourier relationship between the attenuated echo signal in q-space and the spin-displacement PDF is strictly valid only when the narrow pulse assumption ($\delta << \Delta$) is met. In practice, it is difficult to generate $\delta << \Delta$ on a clinical scanner with 40-60 mT/m gradient strength. As a consequence, the diffusion distance is usually slightly underestimated (9, 59, 60). It is for this reason that the effective diffusion time used to estimate the MDD takes the reduced value of $\Delta - \delta/3$ (13). The ADC parallel to the CC is a useful upper bound MDD estimate for all voxels. This estimated MDD includes about 70% of the spin displacements (34) parallel to the fiber orientation and all of the spin displacements perpendicular to the fiber orientation. It is more accurate to use a voxel-specific and direction-dependent estimate of the ADC to constrain the PDF integration length. In practice, this could be incorporated into a DSI reconstruction software package. One practical issue for estimating the ADC using DSI data is that the DSI data often includes very few DWIs to be in the Gaussian regime and among these DWIs an even more limited number of unique diffusion encoding directions. Ideally, only DWIs in the Gaussian

regime should be included in a tensor fit. If only DSI data is available then the DWIs used for the MDD estimate should include measurements made with b-values under a threshold to ensure a sufficient number of unique diffusion encoding directions and sufficient SNR. We fit tensors using subsets of the two *in vivo* DSI-11 data with different b-value thresholds and found that a cut-off around 1500-2000 s/mm^2 provided estimates of the principal eigenvalue along a white matter tract that were consistent with literature (1.2-1.7×10^{-3} mm^2/s (61)). The optimal cut-off point is not clear but this approach appears to provide reasonable compromise between unique diffusion encoding directions, SNR and limiting non-Gaussian effects.

Improving ODF Reconstruction

Truncating q-space at a non-zero signal intensity contaminates the PDF by convolving the true PDF with a point spread function (PSF) after the Fourier transform. The main lobe of the PSF blurs the PDF, determining the PDF resolution ($1/2q_{max}$) and rendering the ODF less sharp. Canales-Rodríguez et al. deblurred the measured PDF using a model free deconvolution method to sharpen the PDF and ODF (35). The side lobes of the PSF cause the Gibbs ringing in the PDF, which translates into severe artifacts in the ODF that hamper the accurate identification of orientational information in a voxel and lead to tractography errors. We have demonstrated that the Gibbs ringing in the PDF is the major source of ODF artifacts.

The most straightforward method to resolve Gibbs ringing is to acquire a larger q-space coverage such that the diffusion signal decays nearly to zero at the q-space edge, which is a common k-space practice. For our DSI-17 *ex vivo*, DSI-11-Gmax225 and DSI-11-Gmax40 *in vivo* data, the average signals at the b_{max} of voxels from the center CC are about 32%, 5% and 11% of the non-diffusion-weighted signals parallel to the CC and 42%, 32% and 40% of the non-diffusion-weighted signals perpendicular to the CC. One major consideration for increasing q-space coverage is the increase in scan time of the already lengthy DSI scan and the impact of noise from the very low SNR measurements at even higher q-values. Additional high q-value measurements are not effective if the signals at the q-space edge reflect only the rectified noise floor (65).

Another approach to minimize Gibbs ringing is to multiply the q-space signal by a window function (apodization function). This method is also commonly used on k-space data (15, 66, 67) although for three- and higher-dimensional NMR experiments, alternatives to the Fourier transform such as the filter diagonalization and maximum entropy methods are used to generate spectra without ringing (68). However, as shown in Fig. 3, the ringing is not fully suppressed after windowing, despite the fact that the adopted Hanning and Blackman filters attenuate the q-space signal to zero at q_{max}. The ODFs reconstructed after q-space apodization reflect this and are still noisy because the common practice of weighting the PDF by the square of the displacement distance for ODF sharpening re-amplifies any remaining ringing. Another drawback of the q-space apodization approach is the loss of high frequency information that contributes details to the PDF and ODF and the effectively wasted scan time spent acquiring these high q-value data.

Extrapolating the q-space data to higher q-values is another approach to bring the signal smoothly down to zero at the q-space edge (31, 32, 37, 38). This method is more computationally intensive than a normal DSI reconstruction. Further, the extrapolation requires fitting the data to a model, while the model-free nature of DSI is often considered to be favorable.

In this study, we demonstrated that limiting the integration length over the PDF to the estimated MDD of the tissue is a useful way to avoid Gibbs ringing from translating into artifacts in the ODF. Specifically, assuming an $N\times N\times N$ (N is an odd integer) q-space grid zero-padded to $N_0\times N_0\times N_0$ (N_0 is an odd integer) grid, the end point on the discrete grid for the PDF integration is calculated as:

$$r_{end}=\frac{MDD}{FOV}\cdot(N_0-1) \quad (2)$$

Using Eq. 1 and the relationship between b-value and q-value, this equation can be simplified to:

$$r_{end}=\frac{\sqrt{6Db_{max}}}{\pi}\cdot\frac{N_0-1}{N-1} \quad (3)$$

where D is the ADC parallel to the CC. Integrating the PDF only to the MDD includes the majority of the PDF signal while excluding the ringing and noise at the edge within the FOV. As a consequence, as shown in Fig. 5, it is possible to weight the PDF by the square (or even higher powers) of the displacement distance to enhance the displacements of the fastest diffusing components, from which the orientation contrast is derived, without amplifying the ringing at the edge of the FOV. The reconstructed ODFs are sharper and cleaner. Enhancing the features of the fast diffusing components and avoiding q-space filtering that blurs the PDF and ODF is particularly important in *ex vivo* tissue that has lower diffusion rates and lower anisotropy. This is normally achieved by starting the PDF integration at a distance from the PDF center (by default a discrete distance of 2.1 in a 17×17×17 q-space grid for DSI-11).

Our study provides clear evidence regarding the optimal selection of the integration length in the DSI reconstruction to mitigate the effects of Gibbs ringing. We highlight the importance of adapting the integration length accordingly for *ex vivo* and *in vivo* tissues and for different tissue types to ensure accurate DSI reconstruction. For *ex vivo* data, the optimal integration length is ~30% of the integration length used for *in vivo* tissues. We have also demonstrated, for the first time, why the default practice of integrating the PDF to a discrete distance of 6.1 (0.75×FOV) for a standard *in vivo* human DSI acquisition (i.e., DSI-11 zero-padded to a 17×17×17 q-space grid with a b-value of 6000-8000 s/mm^2) is effective. This default practice is adopted in software packages such as DIPY and DSI Studio (http://dsi-studio.labsolver.org). Previously, Yeh et al. recommended an integration length of 1 to 1.3 times of the MDD of free water (computed with diffusion rate of 2.51×10^{-3} mm^2/s) (34, 36). This recommendation is approximately in agreement with our *in vivo* results but is invalid

for *ex vivo* brain data. Paquette et al. recommended PDF integration starting at 0.4×FOV and ending between 0.7×FOV and the full FOV depending on the SNR. Paquette's results are based on synthetic data and evaluated based on tractography accuracy (33). Our study builds on this prior work by providing empirical data and demonstrating the specific ways in which artifacts propagate through q-space to the PDF and ODF.

Q-Space Sampling Density Requirement

Discrete sampling in q-space leads to replicas of the spin-displacement PDF. The minimum q-space sampling density required to prevent overlapping PDFs can be determined by taking into account the MDD. Specifically, the Shannon-Nyquist sampling theorem requires the FOV to be at least as large as twice the MDD given in Eq. 1:

$$\frac{1}{\Delta q} \geq 2 \cdot MDD \quad (4)$$

This equation can be also described in terms of b-value using the relationship between q-value and b-value as:

$$\frac{N-1}{2} \geq \frac{\sqrt{6Db_{max}}}{\pi} \quad (5)$$

This equation prescribes a requirement in terms of the q-space grid size N (N is an odd integer) and the maximum b-value that needs to be considered in DSI acquisition and analysis. For hybrid diffusion imaging (32, 69) in which diffusion data acquired on multi-shell q-space can be gridded to a Cartesian lattice for DSI analysis, and generalized q-sampling imaging (34), a variant of DSI that mathematically combines the Fourier transform and PDF integration, the q-space sampling density of the data has to meet the requirement specified by Eq. 4 and Eq. 5.

Given the maximum b-values in our experiments (30,000 s/mm^2 for *ex vivo* data, 10,000 s/mm^2 for DSI-11-Gmax225 *in vivo* and 7,000 s/mm^2 for DSI-11-Gmax40 *in vivo* data) and the estimated mean diffusivity in the center of the corpus callosum, the required q-space grid sizes are at least 5×5×5 for *ex vivo* and 9×9×9 for *in vivo*. Considering the side lobes of the potential Gibbs ringing that may extend beyond the MDD, a slightly larger q-space grid is preferred. Therefore, the commonly used DSI-11 q-space grid (11×11×11) is appropriate for a $b_{\max}$ under 10,000 s/mm^2 in an *in vivo* DSI experiment. Due to SNR constraints, *in vivo* DSI is rarely used with a b-value greater than 10,000 s/mm^2 and therefore insufficient sampling density is unlikely to be the cause of aliasing artifacts for *in vivo* DSI experiments. These q-grid size requirements are in agreement with prior studies that looked at the optimal $b_{\max}$ for a fixed 11×11×11 grid size (22).

For *ex vivo* tissue that has a slower diffusion rate and a shorter mean displacement, the q-space sampling density requirement is much lower theoretically. However, a decrease in q-space grid size also results in a decrease in angular resolution which is a critical issue. For

Cartesian q-space grid constrained in a sphere of sizes from 1×1×1 to 17×17×17, there are 1, 6, 26, 90, 134, 258, 410, 494 and 690 q-space samples on the outer shell. Acquiring less data also results in lower SNR of the combined DSI dataset and therefore potentially influences the quality of DSI results even when the sampling density requirements are satisfied. Therefore, the DSI-11 q-space grid is a suitable trade-off of q-space sampling density, SNR and angular resolution in both *in vivo* and *ex vivo* DSI experiments.

In summary, this study analyzes DSI data with a higher q_{max} and q-space grid size than has previously been presented in whole, human brains. We used the unique *ex vivo* and *in vivo* DSI data to study the effects of q-space truncation and sampling on the PDF and ODF, in an attempt to provide guidelines for the optimal integration length over the PDF that minimizes Gibbs ringing artifacts (Eq. 2 and Eq. 3) and the required q-space sampling density to avoid aliasing in the PDF (Eq. 4 and Eq. 5). Equation 3 provides a formalism for calculating a suitable integration length given a q-space grid size, zero-padded q-space grid size and the maximum b-value. Equation 5 provides a formalism for calculating an upper bound for the maximum b-value for a given q-space grid size or a lower bound for the q-space grid size given a maximum b-value. For in vivo acquisitions acquired with the most commonly used 11×11×11 grid size, Equations 2-5 indicate that a maximum b-value under 10,000 s/mm^2 should provide a PDF that is free of aliasing artifacts and an integration length of around 5 should avoid most Gibbs ringing if the unfiltered q-space data is zero-padded to a 17×17×17 grid. The effects of different amounts of q-space truncation on the PDF and ODF is another important consideration that was not explored in the current study. Further, a full optimization of DSI requires a more comprehensive comparison and evaluation of q_{max}, q-space grid size and q-space filtering parameters. Testing the efficacy of voxel-specific and direction-dependent estimates of MDD to limit the integration length of the PDF would also offer potential further improvements to ODF reconstruction.

CONCLUSION

Gibbs ringing was observed in the PDF of both *ex vivo* and *in vivo* data, resulting in obscured orientations in the ODFs. Using unfiltered q-space data but constraining the integration length over the PDF to around the MDD of the experimental tissue was demonstrated to be a preferred way to reconstruct more accurate and sharper ODFs. For *in vivo* DSI, aliasing of the PDF is unlikely to occur for the commonly used DSI-11 acquisition with a maximum b-value under 10,000 s/mm^2. For *ex vivo* DSI, the sampling density requirement is significantly lower since *ex vivo* tissue has a lower diffusion rate and shorter MDD. However, when taking into account angular resolution and SNR considerations, the DSI-11 acquisition is well-suited to both *ex vivo* and *in vivo* DSI experiments. In conclusion, the data and analysis presented here clarify guidelines for acquiring and reconstructing DSI data such that Gibbs ringing is minimized and subsequent fiber tracking is as accurate as possible.

ACKNOWLEDGEMENTS

We thank Drs. Larry Wald, Boris Keil and Thomas Witzel for their advice and assistance with the experimental set-up. We thank Drs. John Pauly, Christoph Leuze, Franco Pestilli, Van Wedeen, Ruopeng Wang, Julien Cohen-Adad and Kawin Setsompop for helpful discussions.

Grant sponsor: National Institutes of Health; Grant number: NCRR P41RR14075, NIBIB R01EB006847, NIBIB R00EB015445, NIMH/NIBIB U01MH093765, NEI F32 EY022294, NINDS R25NS065743. Grant sponsor: National Science Foundation; Grant number: BCS1228397. Grant sponsor: Canadian Institute of Health Research, Oxford-Stanford Big Data in Biomedicine Seed Grant, Stanford Radiology Angel Funds, Center for Integration of Medicine and Innovative Technology, American Academy of Neurology and American Brain Foundation, Stanford Institute of Neuro-Innovation and Translational Neurosciences, Stanford Neurosciences Institute.

REFERENCES

1. Basser PJ, Mattiello J, LeBihan D. MR diffusion tensor spectroscopy and imaging. Biophysical journal. 1994; 66(1):259–67. [PubMed: 8130344]
2. Pierpaoli C, Basser PJ. Toward a quantitative assessment of diffusion anisotropy. Magnetic Resonance in Medicine. 1996; 36(6):893–906. [PubMed: 8946355]
3. McNab JA, Edlow BL, Witzel T, et al. The Human Connectome Project and beyond: initial applications of 300 mT/m gradients. NeuroImage. 2013; 80:234–45. [PubMed: 23711537]
4. Setsompop K, Kimmlingen R, Eberlein E, et al. Pushing the limits of in vivo diffusion MRI for the Human Connectome Project. NeuroImage. 2013; 80:220–33. [PubMed: 23707579]
5. Van Essen DC, Smith SM, Barch DM, Behrens TE, Yacoub E, Ugurbil K. The WU-Minn Human Connectome Project: an overview. NeuroImage. 2013; 80:62–79. [PubMed: 23684880]
6. Fan Q, Nummenmaa A, Witzel T, et al. Investigating the capability to resolve complex white matter structures with high b-value diffusion magnetic resonance imaging on the MGH-USC connectom scanner. Brain connectivity. 2014; 4(9):718–26. [PubMed: 25287963]
7. Sotiropoulos SN, Jbabdi S, Xu J, et al. Advances in diffusion MRI acquisition and processing in the Human Connectome Project. NeuroImage. 2013; 80:125–43. [PubMed: 23702418]
8. Huang SY, Nummenmaa A, Witzel T, Duval T, Cohen-Adad J, Wald LL, McNab JA. The impact of gradient strength on in vivo diffusion MRI estimates of axon diameter. NeuroImage. 2015; 106(0): 464–72. [PubMed: 25498429]
9. Wedeen VJ, Hagmann P, Tseng WYI, Reese TG, Weisskoff RM. Mapping complex tissue architecture with diffusion spectrum magnetic resonance imaging. Magnetic Resonance in Medicine. 2005; 54(6):1377–86. [PubMed: 16247738]
10. Edlow BL, Takahashi E, Wu O, et al. Neuroanatomic connectivity of the human ascending arousal system critical to consciousness and its disorders. Journal of neuropathology and experimental neurology. 2012; 71(6):531. [PubMed: 22592840]
11. Hagmann, P.; Reese, T.; Tseng, W.; Meuli, R.; Thiran, J.; Wedeen, V., editors. Diffusion spectrum imaging tractography in complex cerebral white matter: an investigation of the centrum semiovale.. Proceedings of the 12th Annual Meeting of ISMRM; Kyoto, Japan. 2004;
12. Wedeen VJ, Wang RP, Schmahmann JD, et al. Diffusion spectrum magnetic resonance imaging (DSI) tractography of crossing fibers. NeuroImage. 2008; 41(4):1267–77. [PubMed: 18495497]
13. Callaghan, PT. Principles of nuclear magnetic resonance microscopy. Clarendon Press; Oxford: 1991.
14. Callaghan PT, Eccles CD, Xia Y. NMR microscopy of dynamic displacements - k-space and q-space imaging. J Phys E Sci Instrum. 1988; 21(8):820–2.
15. Nishimura, DG. Principles of magnetic resonance imaging. Stanford University; 1996.
16. Bracewell, RN.; Bracewell, R. The Fourier transform and its applications. McGraw-Hill; New York: 1986.
17. Tuch, DS. Diffusion MRI of complex tissue structure. Massachusetts Institute of Technology; 2002.
18. Mori S, Crain BJ, Chacko V, Van Zijl P. Three - dimensional tracking of axonal projections in the brain by magnetic resonance imaging. Annals of neurology. 1999; 45(2):265–9. [PubMed: 9989633]
19. Conturo TE, Lori NF, Cull TS, Akbudak E, Snyder AZ, Shimony JS, McKinstry RC, Burton H, Raichle ME. Tracking neuronal fiber pathways in the living human brain. Proceedings of the National Academy of Sciences. 1999; 96(18):10422–7.

20. Tournier J, Calamante F, Connelly A. MRtrix: diffusion tractography in crossing fiber regions. International Journal of Imaging Systems and Technology. 2012; 22(1):53–66.
21. Wedeen VJ, Rosene DL, Wang R, Dai G, Mortazavi F, Hagmann P, Kaas JH, Tseng WY. The geometric structure of the brain fiber pathways. Science. 2012; 335(6076):1628–34. [PubMed: 22461612]
22. Kuo L-W, Chen J-H, Wedeen VJ, Tseng W-YI. Optimization of diffusion spectrum imaging and q-ball imaging on clinical MRI system. NeuroImage. 2008; 41(1):7–18. [PubMed: 18387822]
23. Tian, Q.; Rokem, A.; Edlow, BL.; Folkerth, RD.; McNab, JA. Optimizing q-space sampling density for diffusion spectrum imaging.. Proceedings of the 22nd Annual Meeting of ISMRM; Milan, Italy. 2014; p. 4452
24. Tefera GB, Zhou Y, Juneja V, Narayana PA. Evaluation of fiber tracking from subsampled q-space data in diffusion spectrum imaging. Magnetic resonance imaging. 2013; 31(6):820–6. [PubMed: 23602724]
25. Kuo L-W, Chiang W-Y, Yeh F-C, Wedeen VJ, Tseng W-YI. Diffusion spectrum MRI using body-centered-cubic and half-sphere sampling schemes. Journal of neuroscience methods. 2013; 212(1): 143–55. [PubMed: 23059492]
26. Yeh CH, Cho KH, Lin HC, Wang JJ, Lin CP. Reduced encoding diffusion spectrum imaging implemented with a bi-Gaussian model. IEEE Trans Med Imaging. 2008; 27(10):1415–24. [PubMed: 18815093]
27. Wilkins, B.; Lee, N.; Singh, M., editors. SPIE Medical Imaging. International Society for Optics and Photonics; 2012. Fiber estimation errors incurred from truncated sampling in q-space diffusion magnetic resonance imaging..
28. Paquette M, Merlet S, Gilbert G, Deriche R, Descoteaux M. Comparison of sampling strategies and sparsifying transforms to improve compressed sensing diffusion spectrum imaging. Magnetic Resonance in Medicine. 2015; 73(1):401–16. [PubMed: 24478106]
29. Wu, Y-C.; Alexander, AL. The effects of the finite q-space sampling in diffusion spectrum imaging. Proceedings of the 13rd Annual Meeting of ISMRM; South Beach, Miami, Florida, USA. 2005; p. 576
30. Wu Y-C, Field AS, Alexander AL. Computation of diffusion function measures in-space using magnetic resonance hybrid diffusion imaging. Medical Imaging, IEEE Transactions on. 2008; 27(6):858–65.
31. Yeh C-H, Cho K-H, Lin H-C, Wang J-J, Lin C-P. Reduced encoding diffusion spectrum imaging implemented with a bi-Gaussian model. Medical Imaging, IEEE Transactions on. 2008; 27(10): 1415–24.
32. Hosseinbor AP, Chung MK, Wu Y-C, Alexander AL. Bessel fourier orientation reconstruction (bfor): An analytical diffusion propagator reconstruction for hybrid diffusion imaging and computation of q-space indices. NeuroImage. 2013; 64:650–70. [PubMed: 22963853]
33. Paquette, M.; Merlet, S.; Deriche, R.; Descoteaux, M., editors. DSI 101: Better ODFs for free!. Proceedings of the 22nd Annual Meeting of ISMRM; Milan, Italy. 2014;
34. Yeh F-C, Wedeen VJ, Tseng W. Generalized q-sampling imaging. IEEE transactions on medical imaging. 2010; 29(9):1626. [PubMed: 20304721]
35. Canales-Rodríguez EJ, Iturria-Medina Y, Alemán-Gómez Y, Melie-García L. Deconvolution in diffusion spectrum imaging. NeuroImage. 2010; 50(1):136–49. [PubMed: 19962440]
36. Garyfallidis E, Paquette M, St-Jean S, Coupé P, Descoteaux M. Deconvolution enhanced Generalized Q-Sampling 2 and DSI deconvolution. ISBI'13, HARDI Reconstruction Challenge. 2013
37. Assaf Y, Cohen Y. Structural information in neuronal tissue as revealed by q-space diffusion NMR spectroscopy of metabolites in bovine optic nerve. NMR in Biomedicine. 1999; 12(6):335–44. [PubMed: 10516615]
38. Cohen Y, Assaf Y. High b - value q - space analyzed diffusion - weighted MRS and MRI in neuronal tissues–a technical review. NMR in Biomedicine. 2002; 15(7 - 8):516–42. [PubMed: 12489099]
39. Shemesh N, Westin C-F, Cohen Y. Magnetic resonance imaging by synergistic diffusion-diffraction patterns. Physical review letters. 2012; 108(5):058103. [PubMed: 22400966]

40. Descoteaux M, Deriche R, Le Bihan D, Mangin J-F, Poupon C. Multiple q-shell diffusion propagator imaging. Medical image analysis. 2011; 15(4):603–21. [PubMed: 20685153]
41. Lätt J, Nilsson M, Malmborg C, Rosquist H, Wirestam R, Ståhlberg F, Topgaard D, Brockstedt S. Accuracy of-Space Related Parameters in MRI: Simulations and Phantom Measurements. Medical Imaging, IEEE Transactions on. 2007; 26(11):1437–47.
42. Schmahmann JD, Pandya DN, Wang R, Dai G, D'Arceuil HE, de Crespigny AJ, Wedeen VJ. Association fibre pathways of the brain: parallel observations from diffusion spectrum imaging and autoradiography. Brain. 2007; 130(3):630–53. [PubMed: 17293361]
43. Takahashi E, Dai G, Wang R, Ohki K, Rosen GD, Galaburda AM, Grant PE, Wedeen VJ. Development of cerebral fiber pathways in cats revealed by diffusion spectrum imaging. NeuroImage. 2010; 49(2):1231–40. [PubMed: 19747553]
44. McNab JA, Jbabdi S, Deoni SC, Douaud G, Behrens TE, Miller KL. High resolution diffusion-weighted imaging in fixed human brain using diffusion-weighted steady state free precession. NeuroImage. 2009; 46(3):775–85. [PubMed: 19344686]
45. Miller KL, McNab JA, Jbabdi S, Douaud G. Diffusion tractography of post-mortem human brains: optimization and comparison of spin echo and steady-state free precession techniques. NeuroImage. 2012; 59(3):2284–97. [PubMed: 22008372]
46. Miller KL, Stagg CJ, Douaud G, et al. Diffusion imaging of whole, post-mortem human brains on a clinical MRI scanner. NeuroImage. 2011; 57(1):167–81. [PubMed: 21473920]
47. Edlow BL, Haynes RL, Takahashi E, et al. Disconnection of the ascending arousal system in traumatic coma. Journal of Neuropathology & Experimental Neurology. 2013; 72(6):505–23. [PubMed: 23656993]
48. Tian, Q.; Leuze, CW.; Tomer, R.; Ferenczi, E.; Zeineh, M.; Deisseroth, K.; McNab, JA. Quantification of 3D microscopic tissue features in CLARITY data for comparison with diffusion MRI.. Proceedings of the 23rd Annual Meeting of ISMRM; Toronto, Ontario, Canada. 2015; p. 2766
49. Keil B, Blau JN, Biber S, Hoecht P, Tountcheva V, Setsompop K, Triantafyllou C, Wald LL. A 64-channel 3T array coil for accelerated brain MRI. Magnetic Resonance in Medicine. 2013; 70(1): 248–58. [PubMed: 22851312]
50. Bodammer N, Kaufmann J, Kanowski M, Tempelmann C. Eddy current correction in diffusion - weighted imaging using pairs of images acquired with opposite diffusion gradient polarity. Magnetic Resonance in Medicine. 2004; 51(1):188–93. [PubMed: 14705060]
51. Jenkinson M, Beckmann CF, Behrens TEJ, Woolrich MW, Smith SM. FSL. NeuroImage. 2012; 62(2):782–90. [PubMed: 21979382]
52. Garyfallidis E, Brett M, Amirbekian B, Rokem A, Van Der Walt S, Descoteaux M, Nimmo-Smith I, Contributors D. Dipy, a library for the analysis of diffusion MRI data. Frontiers in neuroinformatics. 2014:8. [PubMed: 24600385]
53. Laun FB, Kuder TA, Semmler W, Stieltjes B. Determination of the defining boundary in nuclear magnetic resonance diffusion experiments. Phys Rev Lett. 2011; 107(4):048102. [PubMed: 21867047]
54. Aganj I, Lenglet C, Sapiro G, Yacoub E, Ugurbil K, Harel N. Reconstruction of the orientation distribution function in single - and multiple - shell q - ball imaging within constant solid angle. Magnetic Resonance in Medicine. 2010; 64(2):554–66. [PubMed: 20535807]
55. Perez F, Granger BE. IPython: a system for interactive scientific computing. Computing in Science & Engineering. 2007; 9(3):21–9.
56. Stejskal E, Tanner J. Spin diffusion measurements: spin echoes in the presence of a time - dependent field gradient. The journal of chemical physics. 1965; 42(1):288–92.
57. Einstein A. Über die von der molekularkinetischen Theorie der Wärme geforderte Bewegung von in ruhenden Flüssigkeiten suspendierten Teilchen. Annalen der physik. 1905; 322(8):549–60.
58. Johansen-Berg, H.; Behrens, TE. Diffusion MRI: From quantitative measurement to in-vivo neuroanatomy. Academic Press; 2009.
59. Mitra PP, Halperin BI. Effects of finite gradient-pulse widths in pulsed-field-gradient diffusion measurements. Journal of Magnetic Resonance, Series A. 1995; 113(1):94–101.

60. Bar-Shir A, Avram L, Özarslan E, Basser PJ, Cohen Y. The effect of the diffusion time and pulse gradient duration ratio on the diffraction pattern and the structural information estimated from q-space diffusion MR: experiments and simulations. Journal of Magnetic Resonance. 2008; 194(2): 230–6. [PubMed: 18667345]

61. Pierpaoli C, Jezzard P, Basser PJ, Barnett A, Di Chiro G. Diffusion tensor MR imaging of the human brain. Radiology. 1996; 201(3):637–48. [PubMed: 8939209]

62. Jones D, Horsfield M, Simmons A. Optimal strategies for measuring diffusion in anisotropic systems by magnetic resonance imaging. Magnetic resonance in medicine : official journal of the Society of Magnetic Resonance in Medicine / Society of Magnetic Resonance in Medicine. 1999:42.

63. Kingsley PB. Introduction to diffusion tensor imaging mathematics: Part III. Tensor calculation, noise, simulations, and optimization. Concepts in Magnetic Resonance Part A. 2006; 28(2):155–79.

64. Kingsley PB, Monahan WG. Selection of the optimum b factor for diffusion - weighted magnetic resonance imaging assessment of ischemic stroke. Magnetic resonance in medicine. 2004; 51(5): 996–1001. [PubMed: 15122682]

65. Eichner C, Cauley SF, Cohen-Adad J, Möller HE, Turner R, Setsompop K, Wald LL. Real diffusion-weighted MRI enabling true signal averaging and increased diffusion contrast. NeuroImage. 2015

66. Harris FJ. On the use of windows for harmonic analysis with the discrete Fourier transform. Proceedings of the IEEE. 1978; 66(1):51–83.

67. Lowe MJ, Sorenson JA. Spatially filtering functional magnetic resonance imaging data. Magnetic Resonance in Medicine. 1997; 37(5):723–9. [PubMed: 9126946]

68. Keeler, J. Understanding NMR spectroscopy. 2nd ed.. Vol. xiii. John Wiley and Sons; Chichester, U.K.: 2010. p. 511

69. Wu Y-C, Alexander AL. Hybrid diffusion imaging. NeuroImage. 2007; 36(3):617–29. [PubMed: 17481920]

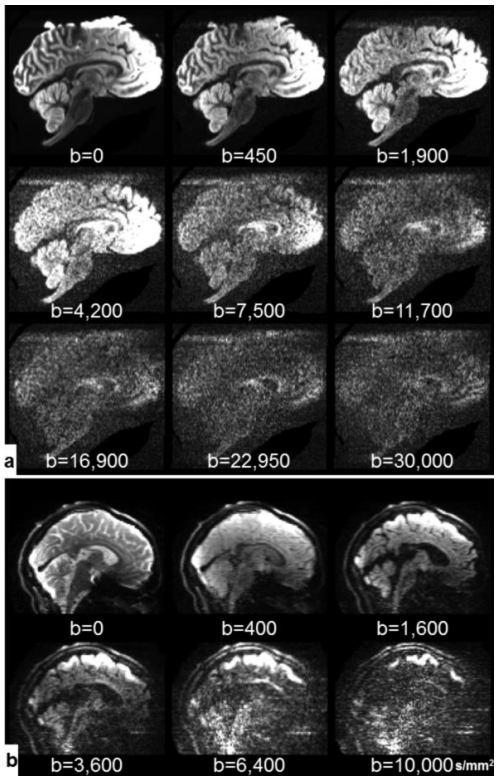

Fig. 1.

Example diffusion-weighted images at various b-values with left-right diffusion-encoding direction for *ex vivo* DSI-17 data (a) and *in vivo* DSI-11-Gmax225 data (b). The images have been individually windowed and leveled for improved visualization.

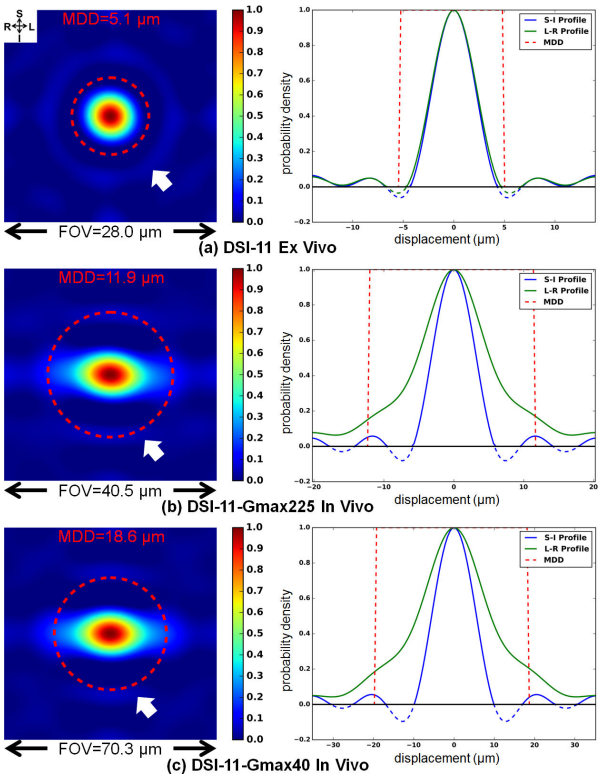

Fig. 2.

Coronal cross-sections through the center of the 3D spin-displacement PDF (left) and the superior-inferior (S-I) and left-right (L-R) profiles through the center of the cross-section (right) for one voxel from the center corpus callosum that has left-right principal orientation for the *ex vivo* DSI-11 (a), *in vivo* DSI-11-Gmax225 (b) and *in vivo* DSI-11-Gmax40 (c) data. Ringing is observed in the PDFs (left, white arrows; right, blue and green curves). The different q-space sampling densities correspond to different PDF field-of-views (FOV). The red dashed circles represent the mean displacement distance (MDD) based on Einstein's equation.

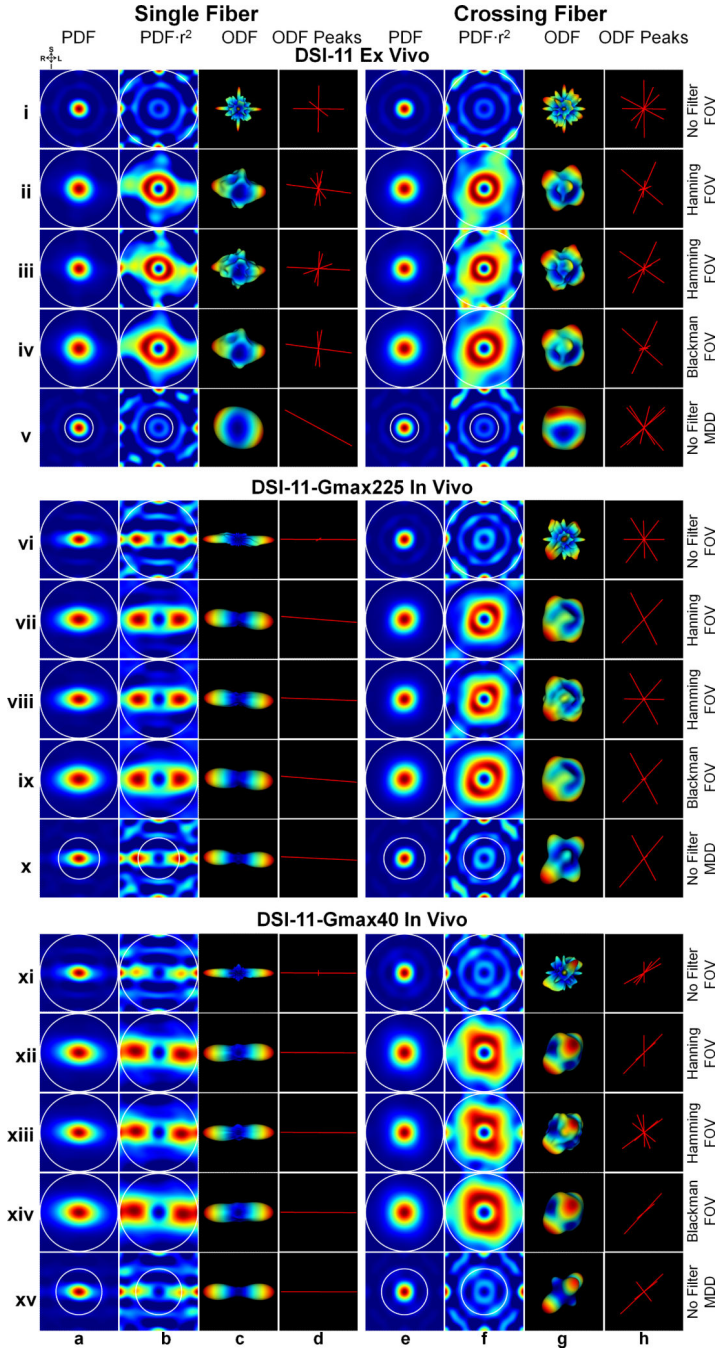

Fig. 3.

Three different ODF reconstruction pipelines for DSI-11 *ex vivo* (rows i to v), DSI-11-Gmax225 *in vivo* (rows vi to x) and DSI-11-Gmax40 *in vivo* data (rows xi to xv). The three pipelines are (1) Unfiltered q-space and integration of the PDF to the full the field-of-view (FOV) (rows i, vi and xi); (2) Filtered q-space and integration of the PDF to the full FOV (rows ii to iv, vii to ix and xii to xiv); (3) Unfiltered q-space and integration of the PDF to the estimated mean displacement distance (MDD) (rows v, x and xv). The single-fiber voxel is from the center corpus callosum. The crossing-fiber voxel is from centrum semiovale (as

shown in Fig. 5e, f and g dashed white boxes). Coronal cross-sections through the center of the 3D spin-displacement PDFs are shown in columns a and e. These same PDFs weighted by the square of the displacement distance are shown in columns b and f. The ODFs that correspond to the PDFs in columns b and f are shown in columns c and g. The local maximas (peaks) detected from the ODFs are shown in columns d and h. The white circles represent the integration distance. The color map for both the PDFs and ODFs represents low to high values as blue to red.

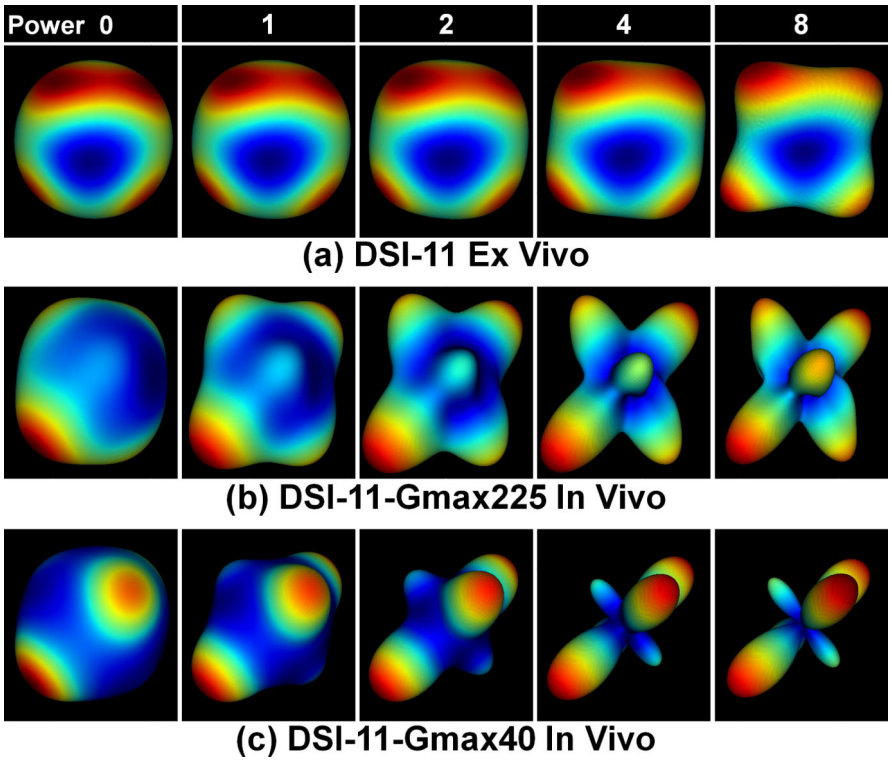

Fig. 4.

An example of the effects of weighting the PDF by different powers, i.e. 0, 1, 2, 4 and 8, of displacement distance on the reconstructed ODF. The crossing-fiber voxel is from centrum semiovale (as shown in Fig. 5e, f and g dashed white boxes). The color map represents low values (blue) to high values (red) in the ODF.

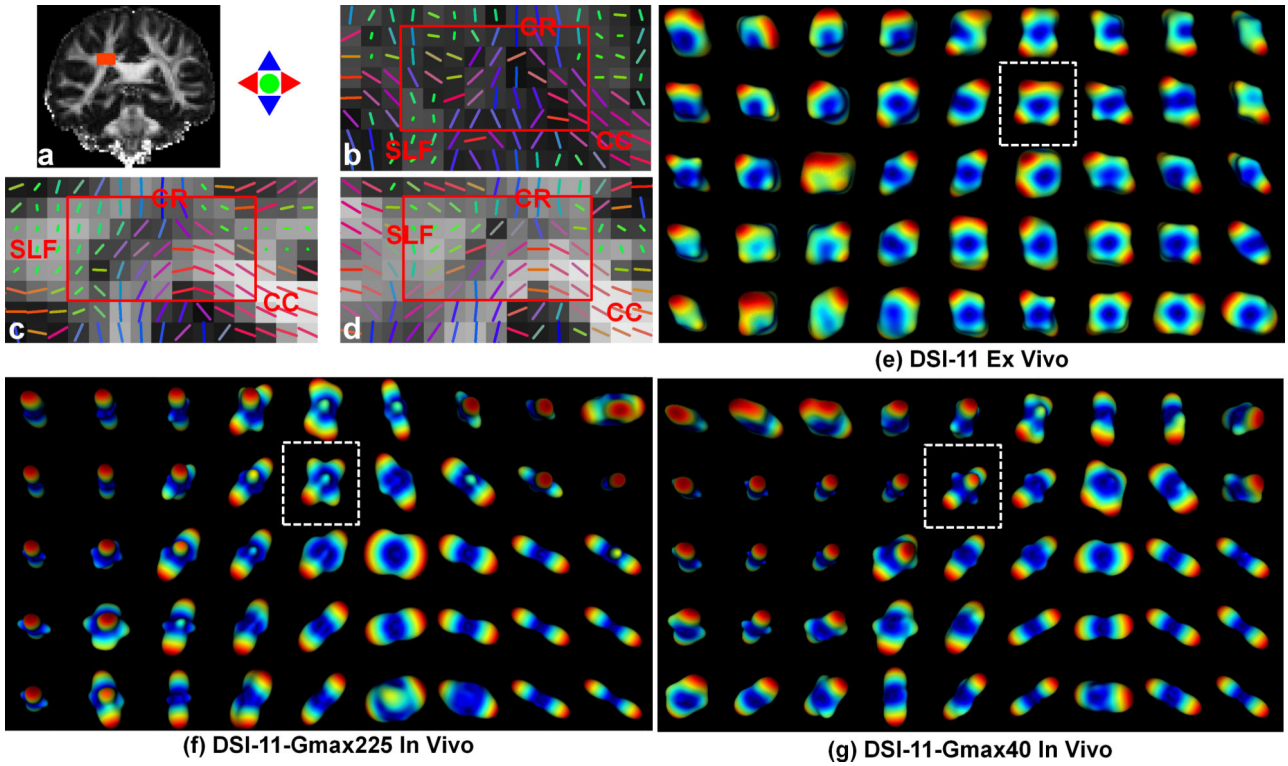

Fig. 5.

Reconstructed tensors and ODFs from centrum semiovale ROI (a) containing the corpus callosum (CC), the corona radiata (CR) and the superior longitudinal fasciculus (SLF) for the *ex vivo* DSI-11 (b and e), *in vivo* DSI-11-Gmax225 (c and f) and *in vivo* DSI-11-Gmax40 data (d and g). The primary eigenvectors of tensors were plotted over the fraction anisotropy maps (b to d). The PDFs were weighted by the displacement distance to the power of 8 for the *ex vivo* data (e) and to the power of 2 for the *in vivo* data (f and g) for the ODF reconstruction, which integrates the weighted PDFs to the estimated mean diffusion distance. The white dashed boxes in (d and e) indicate the crossing-fiber voxels presented in Fig. 3 and 4. The ODF color map represents low values as blue to high values as red in ODF.

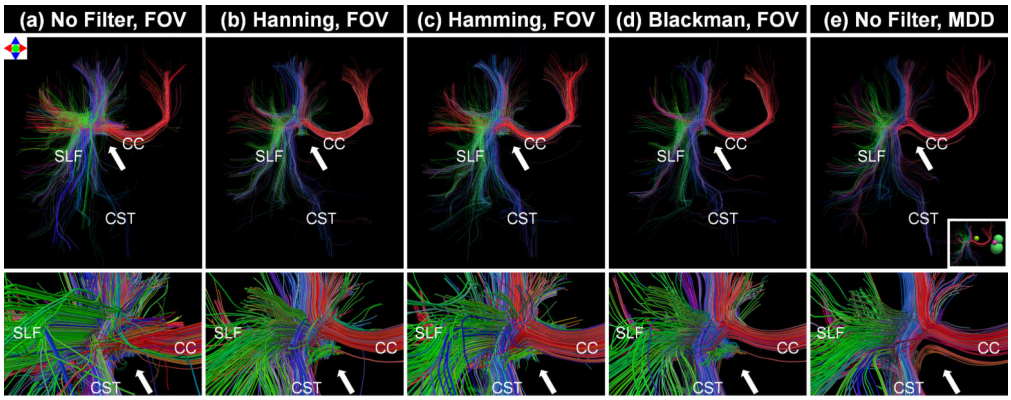

Fig. 6.

Deterministic tractography results shown from an anterior view (top row) and anterior zoomed view (bottom row) for the three ODF processing pipelines from the DSI-11-Gmax40 *in vivo* data. The three pipelines are (1) Unfiltered q-space and integration of the PDF to the full the field-of-view (FOV) (column a); (2) Filtered q-space and integration of the PDF to the full FOV (columns b to d); (3) Unfiltered q-space and integration of the PDF to the estimated mean displacement distance (MDD) (column e). The tractography results were generated using the centrum semiovale ROIs shown in Fig. 5 as a seed mask. The inset figure shows four spherical exclusion masks placed to eliminate cingulum and contralateral tracts for ease of interpretation. Streamlines are color-coded according to the direction of their middle segment (red: medial-lateral; green: anterior-posterior; blue: superior-inferior).

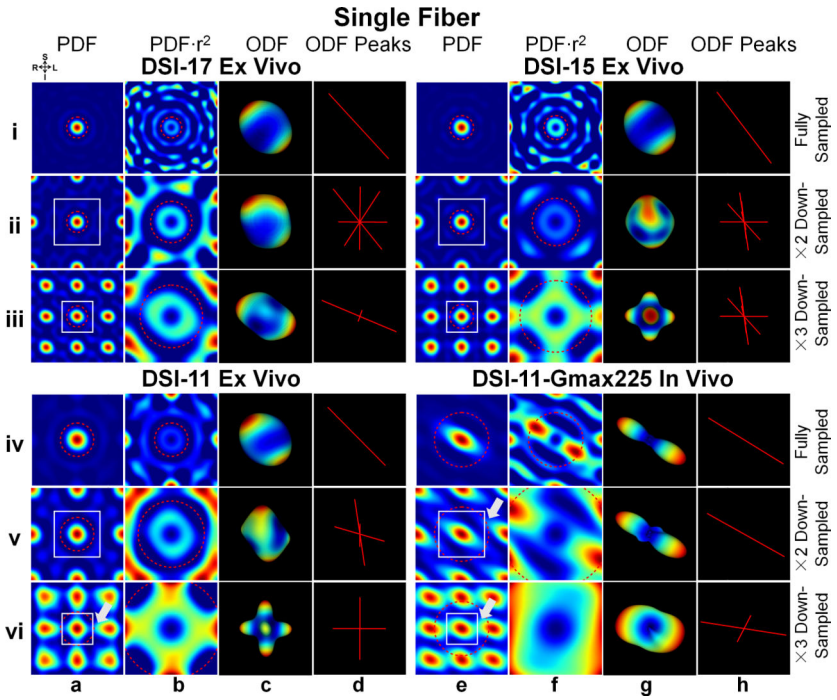

Fig. 7.

The PDF, weighted PDF, ODF and ODF peak for the fully sampled (rows i and iv) and down-sampled (rows ii and v by a factor of 2, rows iii and vi by a factor of 3) q-space signal from a voxel in the corpus callosum of the three *ex vivo* (DSI-11, DSI-15 and DSI-17) and one *in vivo* (DSI-11-Gmax225) datasets. Coronal cross-sections through the center of the 3D spin-displacement PDFs are shown in columns a and e. The spatial extent over which the PDF was plotted is kept constant across different down-sampling schemes. The portion of these same PDFs in the field-of-view (FOV, represented by white boxes) is weighted by the square of the displacement distance and shown in columns b and f. All ODFs were reconstructed using unfiltered q-space signal and integrating the PDF to either the estimated mean displacement distance (MDD, red dashed circles) or the new FOV after down-sampling if it is smaller than MDD (i.e. row vi, column b; rows v and vi, column f). The ODFs that correspond to the PDFs in columns b and f are shown in columns c and g. White arrows indicate the regions of aliasing artifacts in the PDF. The color map represents low values (blue) to high values (red) in both the PDF and ODF.

Table 1

Data acquisition parameters.

Acquisition	In Vivo		Ex Vivo		
Parameters	**DSI-11-Gmax225**	**DSI-11-Gmax40**	**DSI-11**	**DSI-15**	**DSI-17**
Δ/δ^{*}(ms)	20.9/12.9	49.2/42.3	29.4/16.7		
G_{max}(mT/m)	225	40	252		
b_{max}(s/mm^2)	10,000	7,000	30,000		
$q_{max}/\Delta q$(mm^{-1})	123.5/24.7	71.1/14.2	178.5/35.7	178.5/25.5	178.5/22.3
q-sample #	515	515	515	1419	2109
TE/TR(ms)	47/5900	106/6900	65/13300		
Resolution(mm^3)	2 × 2 × 2	2.5 × 2.5 × 2.5	1.5 × 1.5 × 1.5		
FOV(mm^2)	220 × 220	220 × 200	180 × 138		
Slice #	80	52	112		
Partial Fourier	6/8	6/8	6/8		
GRAPPA R	3	3	2		
BW(Hz/pixel)	2526	2470	1985		
Echo spacing(ms)	0.53	0.51	0.53		
Scan time(min)	55	55	120	330	490

*Note that δ includes the time from the start of the ramp up to the strongest gradient strength used for the diffusion encoding pulse until the start of the ramp down.